

Investigating wave data from the FAST satellite by reconstructing the wave distribution function

G. Stenberg and T. Oscarsson

Department of Theoretical Physics, Umeå University, Umeå, Sweden

M. André

Swedish Institute of Space Physics, Uppsala Division, Uppsala, Sweden

C. C. Chaston

Space Sciences Laboratory, University of California, Berkeley, California, USA

Received 16 August 2001; accepted 24 September 2001; published 15 August 2002.

[1] We study wave measurements made by the FAST satellite at 4100-km altitude in the auroral region. Three electric and three magnetic wave field components are available, and wave emissions appear close to the local proton gyrofrequency (187 Hz) and at its harmonics. The particle observations reveal an electron beam as well as counterstreaming protons and oxygen ions. The plasma density is very low. We investigate the linear wave mode structure using a five-component bi-Maxwellian plasma model. The streaming electrons cause an instability at large perpendicular wave vectors. Using cross spectra and autospectra computed from the data, we reconstruct the wave distribution function (WDF). The results show that the observations are consistent with a linear description of the plasma. We find a good agreement between the reconstructed wave energy distribution, and the instability and our analysis gives a wavelength of ~ 2.5 km. The reconstructed WDF fits into a simple geometrical picture, where the satellite is passing through the outer edge of a region with precipitating electrons. *INDEX TERMS:* 2704 Magnetospheric Physics: Auroral phenomena (2407); 2772 Magnetospheric Physics: Plasma waves and instabilities; 2716 Magnetospheric Physics: Energetic particles, precipitating; 2753 Magnetospheric Physics: Numerical modeling; *KEYWORDS:* auroral region, electron beams, ion cyclotron waves, wave polarization, wave distribution function, wave propagation

1. Introduction

[2] Waves with frequencies at or slightly above the local proton gyrofrequency (f_{cH^+}) are commonly observed on auroral field lines. Observations are not limited to a certain altitude, but waves are detected from altitudes of a few thousand kilometers to several Earth radii [e.g., André *et al.*, 1987; Cattell *et al.*, 1991; Chaston *et al.*, 1998]. One type of waves is usually observed in regions with low density and together with ion beams and field-aligned currents. The field fluctuations occur mainly perpendicularly to the background magnetic field, and sometimes their power spectra exhibit a harmonic structure with emissions at higher multiples of f_{cH^+} as well [Kintner *et al.*, 1979; Chaston *et al.*, 1998]. Generally, these ion cyclotron waves are believed to be electrostatic, although recent observations indicate that they include a magnetic component [Chaston *et al.*, 1998].

[3] Several mechanisms have been suggested to generate ion cyclotron waves. Sources of free energy are not difficult to find as these waves often are accompanied by ion beams and/or electron beams. Some studies favor

generation by ion beams [Kintner *et al.*, 1979; Kaufmann and Kintner, 1982; André *et al.*, 1987], while other point toward current-driven instabilities [Bergmann, 1984; Cattell *et al.*, 1998; Chaston *et al.*, 2002]. Chaston *et al.* [2002] propose that the exact particle distribution is essential for explaining the instability. Recently, it has been suggested that gradients in parallel ion beam velocities play a major role in the generation of ion cyclotron waves [Gavriushchaka *et al.*, 2000].

[4] Ion cyclotron waves play an important role in the transfer of energy between different particle populations in the auroral region and could for example cause ion heating. To understand the details of the energy transfers involving ion cyclotron waves, it is necessary not only to determine the frequencies but also the wave vectors. Since the space plasma is highly dispersive, the wave vector is closely linked to the wave polarization. Attempts have been made to investigate the polarization properties of ion cyclotron waves, but usually only one or two of the available polarization parameters are considered, e.g., E/B or E_{\parallel}/E_{\perp} [Bergmann, 1984; Chaston *et al.*, 2002]. In this study we will utilize all relevant polarization information available in a representative ion cyclotron wave event observed by the FAST satellite [Carlson *et al.*, 1998].

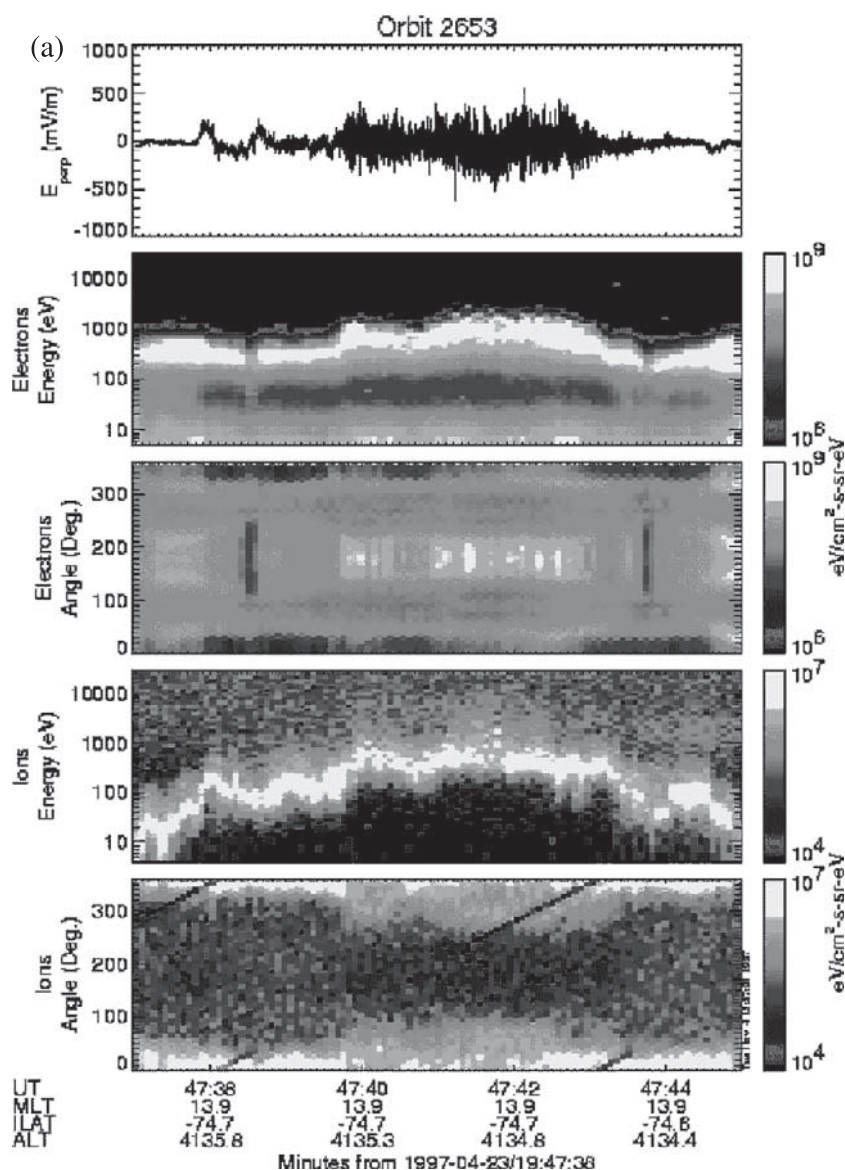


Figure 1. (a) Field and particle data recorded by the FAST spacecraft above the dayside auroral oval [from *Chaston et al.*, 1998]. See section 2 for explanation. (b) The power spectrum of the perpendicular electric field show wave emissions close to the harmonics of f_{cH^+} (187 Hz). (c) The power spectrum of the perpendicular magnetic field also reveals wave emissions at f_{cH^+} and its multiples. The power in the magnetic field peaks below the multiples, while the power in the electric field peaks at or slightly above.

[5] We use a maximum entropy method to reconstruct the wave distribution function (WDF) from the observed frequency spectra [Oscarsson, 1994]. The WDF can be seen as the wave energy distribution in wave vector space. FAST provides three electric and three magnetic field components and is thus well suited for polarization investigations. The event subject to our study was observed by the FAST satellite at 4100 km altitude on 23 April 1997 and show the typical situation with wave emissions at multiples of the proton gyrofrequency. Simultaneously, the particle measurements reveal a low density together with upgoing ion beams and electrons traveling downward (Figure 1a). This particular event has already been analyzed by *Chaston et al.* [1998]. The purpose of our paper is to extend this study by using WDF analysis to determine if the observed spectra are

consistent with a linear description of the plasma. Also, from our estimate of the WDF we obtain the direction and magnitude of a typical wave vector.

2. Observations

[6] Figure 1a shows observations from a FAST crossing of an ion beam region at 4100-km altitude and in the dayside auroral oval. The first panel shows the electric field measured along the spacecraft trajectory (roughly northward) and perpendicular to the geomagnetic field. The electric field data shown here have been recorded with a sample rate of 8192 Hz from orthogonal dipole pairs in the spacecraft spin plane [Ergun *et al.*, 2001]. Since the spacecraft at this time is in the winter hemisphere the

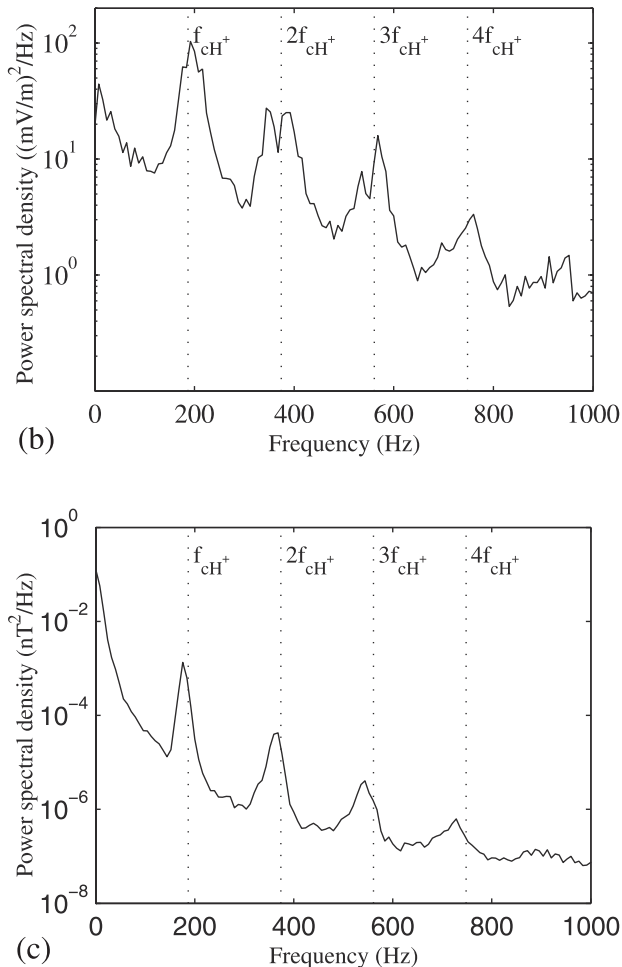


Figure 1. (continued)

auroral oval below is in darkness and a quasi-static potential drop exists providing inverted-V electrons and an upgoing ion beam as shown in the particle data in the remainder of this figure. These data were measured by the FAST electron electrostatic analyzer (EESA) and ion electrostatic analyzer (IESA) experiments [Carlson *et al.*, 2001] with a resolution of 80 ms. The second and third panels show that the electrons have energies up to 1 keV and at that time when the waves are observed the electrons are strongly field aligned within the source cone as indicated by the enhanced differential energy flux at a pitch angle of 180° from 1947:40 to 1947:43 UT. These electrons are strongly modulated by the wave field as has been demonstrated by *McFadden et al.* [1998] and reach the ionosphere to cause flickering aurora. The ion data shown in the lower two panels are dominated by the ion beam streaming upward along the field line ($0^\circ/360^\circ$) with energies comparable to that of the downgoing electrons. These ions are heated most likely through a cyclotron resonance with the wave to yield the somewhat more diffuse ions over the same interval where the field-aligned electrons occur.

[7] The wave spectra shown in Figures 1b and 1c represent averages over the interval of most intense wave activity shown in Figure 1a. These show peaks in wave power very close to multiples of the proton cyclotron

harmonics indicated by the vertical lines in this figure. Interestingly, these peaks are observed in both the electric and magnetic field spectra and occur at slightly different frequencies. The power in the magnetic field peaks below f_{cH^+} , whereas the power in the electric field peaks at or above f_{cH^+} .

[8] Table 1 shows the results from a moment analysis of the electron and ion distributions that will be used as a basis to model the plasma in the remainder of this report. These follow from averaged electron and ion data over the interval of most intense wave activity from 1947:40 to 1947:43 UT. The beam electron component has been isolated in the integration by including only fluxes within the source cone (150° – 210°). Since the distribution is both field aligned within this angular range and is distinct in temperature from the plasma sheet at these times this approximation seems reasonable and adequate for the bi-Maxwellian based modeling to follow. The parameters for the plasma sheet electron component are obtained by integrating over the remainder of the electron distribution above 20 eV to eliminate the effects of spacecraft photoelectrons. A similar approach is adopted for the ion distributions where the beam component moments are found from integration over the loss cone width using the TEAMS mass spectrometer instrument [Klumpar *et al.*, 2001]. The plasma sheet moments are determined from the remaining pitch angles under the assumption that all plasma sheet ions are protons from the IESA experiment. The densities of the ions are then adjusted proportionally with reference to an integration over the entire ion distribution measured by the IESA and EESA instruments to ensure that the plasma is charge neutral.

3. Stability Analysis

[9] Ion cyclotron waves are previously studied by using a bi-Maxwellian plasma model [Cattell *et al.*, 1998], and we choose this approach as well. Thus, on the basis of the observations described in the previous section we model the plasma using bi-Maxwellian distributions. The plasma model is summarized in Table 1. We distinguish five different plasma components. For the ions we consider a hot plasma sheet proton component, a proton beam, and an oxygen beam. The electrons are modeled using a hot plasma sheet component and a cold beam.

Table 1. Plasma Model^a

	n, cm^{-3}	T_{\parallel}, eV	T_{\perp}, eV	v_d/v_{th}
H^+	0.1	5000	5000	0
H^+	0.45	100	200	-2.9
O^+	0.45	100	200	-2.9
e^-	0.7	1000	1000	0
e^-	0.3	100	100	2.35

^aThe plasma model is based on the observations presented in section 2. The columns show density (n), parallel (T_{\parallel}) and perpendicular (T_{\perp}) temperature, and drift velocity for each of the five plasma components. The drift velocity is expressed as the ratio between the actual drift velocity (v_d) and the parallel thermal velocity (v_{th}) for each component. The different signs indicates that the electrons move antiparallel to the background magnetic field, whereas the ions beams are parallel. Here parallel and perpendicular refer to directions relative to the background magnetic field.

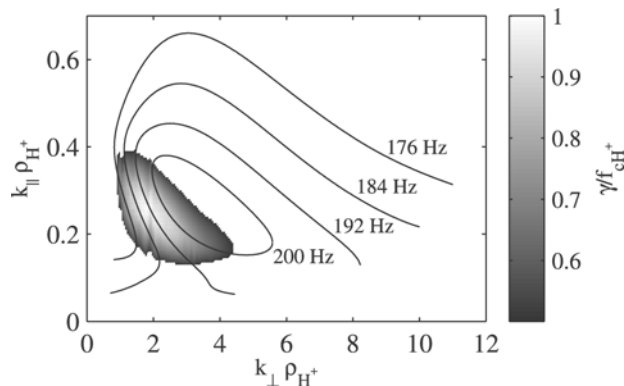


Figure 2. The solution to the dispersion relation as a function of normalized wave vector component parallel (k_{\parallel}) and perpendicular (k_{\perp}) to the background magnetic field. Here ρ_{H^+} is the gyro radius of the hot protons and $\rho_{H^+} = 830$ m. The different curves correspond to contours of constant frequency. The solution is shown in the plasma frame of reference and the proton gyrofrequency is 187 Hz. The temporal growth rate is color coded and placed on top of the dispersion curves. Only the region of largest growth is shown.

[10] We use the computer code WHAMP [Rönmark, 1982] to solve the dispersion relation for linear waves and investigate the wave mode structure. Figure 2 shows a growing wave mode that we find near f_{cH^+} for large perpendicular wave vectors. Contours of constant frequency as well as color coding for the temporal growth rate are plotted versus normalized parallel (k_{\parallel}) and perpendicular (k_{\perp}) wave vector components.

[11] It is clear that the instability is caused by the streaming electrons. Removing the ion beams by setting $v_d = 0$ does not remove the instability but only causes minor changes to the real part of the frequency. On the other hand, removing the drifting electrons also removes the instability. The maximum growth rate is $0.14f_{cH^+}$ and occur very close to f_{cH^+} .

[12] The dispersion solver finds a growing wave mode also at the second harmonic, but the extension of this mode is restricted to a smaller part of wave vector space. We are unable to find unstable waves at higher multiples using the model in Table 1. To reproduce higher multiples, it is probably necessary to introduce more detailed particle distributions [Chaston *et al.*, 2002] or velocity gradients [Gavrishchaka *et al.*, 2000]. However, in this study we are primarily interested in the polarization properties of the wave and concentrate on the emission near the fundamental resonance at f_{cH^+} . We believe that the polarization properties close to f_{cH^+} do not change considerably by invoking small changes in the model to better capture the emissions at higher multiples.

[13] Theoretically, the growing wave mode displays a value of E/B that varies strongly, from values below the speed of light (c) to $1000c$, and generally, the wave becomes more electrostatic for larger k_{\perp} . The observed E/B ranges from $0.75c$ to $6c$ which, at least for frequencies below f_{cH^+} , is consistent with the theoretical prediction. Above f_{cH^+} , comparisons with the data indicate that the observed mag-

netic field component is somewhat larger than predicted by linear theory. E_{\perp}/E_{\parallel} is also varying over the dispersion curves but is comparable to the 6–11 suggested by the data. Similar results are found also by Chaston *et al.* [2002], and from this it seems that linear theory is well capable of explaining the observed waves. However, this analysis is far from complete. E/B and E_{\perp}/E_{\parallel} are not the only parameters defining the state of polarization. In fact, since there are six different field components, counting all mutual amplitude and phase relations there are in total 36 different polarization parameters. In order for linear plasma theory to explain the waves the observations of all these parameters must be consistent with the theoretical predictions. Therefore our aim with this study is to include as many polarization parameters as possible in the analysis and thus investigate if the wave observations are fully consistent with our model and linear theory.

[14] The presence of different beams in the system indicates that there may be other growing modes near multiples of f_{cH^+} . Indeed, removing the ion drifts (setting the drift speed to 0) and keeping all other parameters constant reveals a fast growing broadband ion acoustic-like mode extending from $k_{\perp} = 0$ to perpendicular wave vectors comparable to what we have for the growing mode described above. These ion acoustic-like waves are growing for electron drifts up to $v_d/v_{th} = 2.4$ with maximum growth occurring for a drift equal to $v_d/v_{th} = 1.7 - 1.8$. Introducing the oxygen beam causes very small differences. The hydrogen beam, however, changes the situation. Turning on this beam by successively increasing the drift velocity lowers the frequency of the ion acoustic mode. For drifts in our model the frequency is suppressed below $0.1f_{cH^+}$.

[15] For higher electron beam velocities ($v_d/v_{th} > 2.5$) we find a rapidly growing broadband beam-like mode. This mode seems to be unaffected by the ion beams. However, if the electron beam velocity is smaller than $2.5v_{th}$, this mode does not result in broadband growth.

[16] During the observed wave event the satellite is in a density cavity where no cold plasma is believed to be present [McFadden *et al.*, 1999]. Adding cold plasma to the model changes the situation considerably. Introducing only a small fraction of 1 eV electrons, say 1% of the total density, results in broadband growth. Since no such broadband waves are observed we find it reasonable to use a model with no cold plasma.

[17] There are also nongrowing modes near f_{cH^+} . We numerically find the mode that for higher frequencies usually is called the whistler mode [André, 1985]. However, it reaches below f_{cH^+} and is therefore included in our analysis. The whistler mode is right circularly polarized for $k_{\perp} = 0$ and frequencies near f_{cH^+} . Below f_{cH^+} , we find another mode that is left circularly polarized for $k_{\perp} = 0$ and frequencies near f_{cH^+} . This mode does not exist above the proton gyrofrequency, but it is included when we consider frequencies less than f_{cH^+} .

[18] In summary, we have found a growing wave mode with characteristics that at first sight agrees well with the observations. We will continue our analysis by systematically comparing all relevant polarization information in the observations with the polarization of the theoretically predicted wave mode. We do this by reconstructing the wave

distribution function using a maximum entropy method described in the next section.

4. Reconstruction Scheme

[19] The purpose of our wave distribution function (WDF) analysis is to use the polarization information in the data to find a wave energy distribution in \mathbf{k} space that is consistent with the data. We define the WDF $\psi(\mathbf{k})$ as the energy density in wave vector space. Formally, the WDF is defined as

$$\psi(\mathbf{k}) = \mathbf{E}^*(\mathbf{k}) \cdot \left[\frac{1}{\omega} \partial_\omega \mathbf{D}(\omega, \mathbf{k}) \right] \cdot \mathbf{E}(\mathbf{k}). \quad (1)$$

Here $\mathbf{E}(\mathbf{k})$ is the Fourier-transformed electric field, $\mathbf{D}(\omega, \mathbf{k})$ is the dispersion matrix, and the bracket is evaluated at $\omega = \omega(\mathbf{k})$ satisfying $\det \mathbf{D}(\omega, \mathbf{k}) = 0$. Knowledge of the WDF and thereby the wavelengths is important for understanding wave generation and energy transfer processes in space. However, owing to the limited space resolution of space measurements the WDF cannot be measured directly. Instead, we reconstruct the WDF from observed spectral densities. The reconstruction scheme is briefly described below and the reader is referred to *Oscarsson* [1994] for details.

[20] The relation between the spectral densities and the WDF is given by

$$S_{ij}[\omega, \Delta\omega; \psi(\mathbf{k})] = \int_V d\mathbf{k} A_{ij}(\mathbf{k}) \psi(\mathbf{k}) \delta[\omega - \omega(\mathbf{k})]. \quad (2)$$

Here we take into account explicitly the fact that spectral densities are measured with a finite frequency resolution $\Delta\omega$. The integral is taken over the volume in \mathbf{k} space where $\omega - \Delta\omega/2 \leq \omega(\mathbf{k}) < \omega + \Delta\omega/2$. We point this out here since it has some implications later on. However, to keep notations short, we drop both the ω and $\Delta\omega$ dependence in the following discussion.

[21] Note that $S_{ij}[\psi(\mathbf{k})]$ is just one of the possible auto-spectral or cross-spectral densities that can be obtained. To each one, we have a corresponding integration kernel $A_{ij}(\mathbf{k})$. For example, the integration kernel corresponding to the cross-spectrum between the x and y component of the electric field is

$$A_{E_x E_y}(\mathbf{k}) = \frac{e_x(\mathbf{k}) e_y^*(\mathbf{k})}{\mathbf{e}^*(\mathbf{k}) \cdot \left[\frac{1}{\omega} \partial_\omega \mathbf{D}(\mathbf{k}, \omega) \right] \cdot \mathbf{e}(\mathbf{k})}, \quad (3)$$

where the denominator is evaluated at $\omega = \omega(\mathbf{k})$. Furthermore, $\mathbf{e}(\mathbf{k})$ is the polarization unit vector and $e_x(\mathbf{k})$, $e_y(\mathbf{k})$ are the x and y components of the polarization vector. The other possible integration kernels are defined in a similar way. The characteristics of the measuring antennae can also be included in the integration kernels, although it is not in equation (3).

[22] Given the WDF we can use equation (2) to calculate all spectral densities. However, the inverse problem, finding the WDF given all possible spectral densities, is an under-determined problem. There is an infinity of different $\psi(\mathbf{k})$ that correspond to the same spectral densities. To find a

unique solution, we use a maximum-entropy method, where we define an entropy function and among all feasible solutions we choose the one having the largest entropy.

[23] The set of solutions, from which we choose the one with the largest entropy, satisfy the relation

$$\xi[\psi] = \frac{1}{2} \sum_{ij} \frac{|C_{ij} - S_{ij}[\psi]|^2}{\sigma_{ij}^2} \leq \xi_{\text{bound}}, \quad (4)$$

where S_{ij} are the theoretically calculated spectra for a certain ψ , C_{ij} are the observed spectra, and σ_{ij}^2 the corresponding estimated variances. Hence the resulting WDF should produce theoretical spectral densities close to, but not necessarily identical to, the observed spectra. The unavoidable presence of observational errors makes this approach very reasonable. If the errors are random and normally distributed with variances σ_{ij}^2 , $\xi[\psi]$ is χ^2 distributed and we can use this to set an upper bound, ξ_{bound} , on $\xi[\psi]$.

[24] The entropy function, $H[\psi]$, is defined according to

$$H[\psi] = - \int_V d\mathbf{k} \psi(\mathbf{k}) \ln \left[\frac{\psi(\mathbf{k})}{\Psi} \right], \quad (5)$$

where $\Psi = \frac{1}{V} \int_V d\mathbf{k} \psi(\mathbf{k})$. This is not the only possible choice of an entropy function. However, this particular choice means that when the data contain no information on the WDF we obtain a ‘‘flat’’ solution; that is, the energy will be evenly distributed in \mathbf{k} . Choosing another entropy function, we can force the reconstruction to concentrate the wave energy to the area in \mathbf{k} space where maximum growth occur. These so-called biased solutions are presented and discussed in section 6 below.

[25] In summary, the reconstruction scheme can be written as the optimization problem

$$\begin{aligned} &\text{maximize } H[\psi] \\ &\text{subject to } \xi[\psi] \leq \xi_{\text{bound}} \end{aligned} \quad (6)$$

Oscarsson [1994] describes an efficient method for solving equation (6).

5. Results

[26] In this section we present results obtained by applying the reconstruction method to the observations made by FAST. The observational input to the reconstructions are spectral densities for the frequency of interest. We compute the spectral densities using the wave observations made from 1947:40.417 to 1947:43.104 UT. The electric and magnetic fields are sampled with a frequency of 8192 Hz. We average over four points and the effective sampling frequency is reduced to 2048 Hz. The spectral densities are then computed via fast Fourier transforms [e.g., *Bendat and Piersol*, 1971] using a Gaussian window and a record length of 1024 points. The $1/e$ half width of the Gaussian window is $\sqrt{2} \cdot 256$ points. The final spectrum is computed by averaging over 35 time records and 4 frequencies and the resulting frequency resolution is 8 Hz. Reconstructions are made for two different frequencies, one slightly below f_{cH^+} and one slightly above (184 Hz

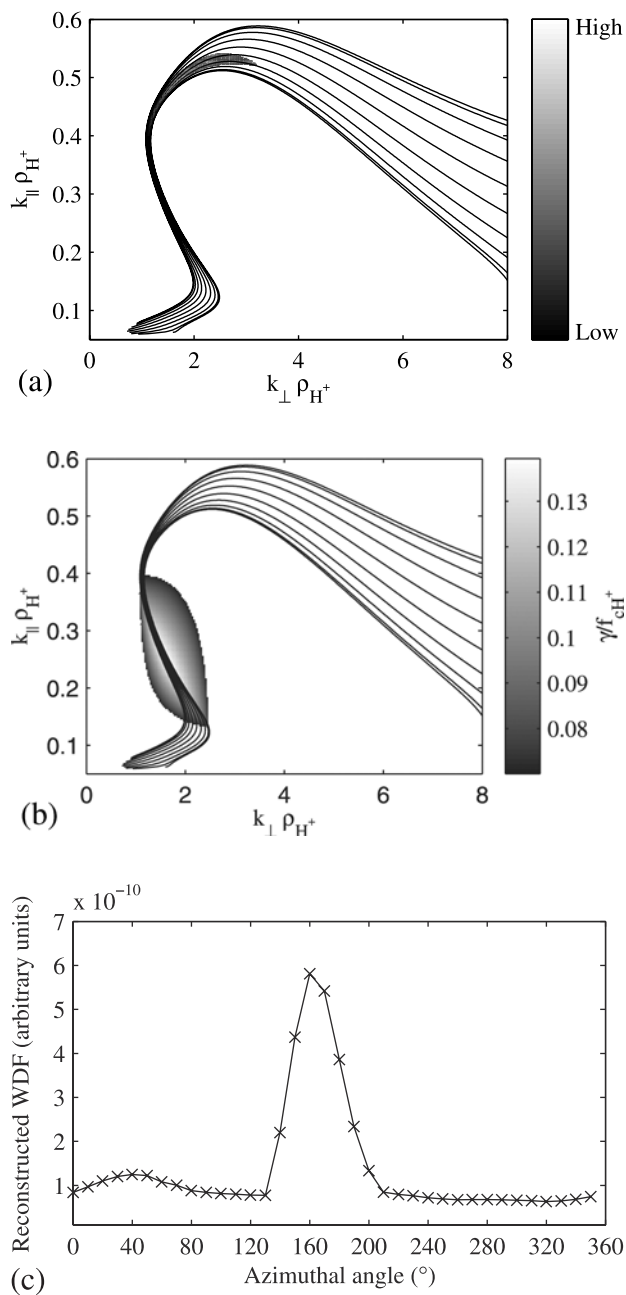


Figure 3. (a) The reconstructed wave distribution function (WDF) (arbitrary units) at frequency $f = 0.983 f_{cH^+}$ (184 Hz) is shown on top of the dispersion relation. In the color code used red corresponds to the highest values blue to the lowest. The maximum is difficult to see but is located at $k_{\perp} \rho_{H^+} = 1.5$ and $k_{\parallel} \rho_{H^+} = 0.47$. The solution to the dispersion relation is shown in the frame of reference of the satellite. Hence the different curves correspond to different directions of k_{\perp} (different ϕ). (b) The temporal growth rate is shown on top of the dispersion curves. Only the curves corresponding to $f = 0.983 f_{cH^+}$ are shown. (c) The reconstructed WDF versus azimuthal angle, ϕ . $\phi = 90^\circ$ is the direction of the satellite velocity.

and 192 Hz). The spectral densities for these two frequencies are presented in Table A1 in Appendix A.

[27] It should be noted that we do not include cross spectra between electric and magnetic field components.

Oscarsson et al. [1997] used the same procedure when analyzing Freja measurements, in order to avoid possible cross-calibration problems due to, for instance, phase shifts in the electronics.

[28] The theoretical input to the reconstruction program is the solution to the dispersion relation for the plasma model described and justified above (Table 1). For the frequencies under consideration we provide the wave vectors satisfying $\omega = \omega(\mathbf{k})$ and the corresponding polarization vectors. The Doppler shift due to the satellite velocity is included, and therefore the solution to the dispersion relation depends on the azimuthal wave vector angle, ϕ , as well.

[29] Figure 3a show the result for $f = 0.983 f_{cH^+}$ (184 Hz). The solid lines show the solution of the dispersion relation as a function of normalized wave vector components parallel (k_{\parallel}) and perpendicular (k_{\perp}) to the background magnetic field. The different curves correspond to constant frequencies in the satellite frame at different azimuthal angles. Note that since the Doppler-shift change with \mathbf{k} , the frequency in the plasma frame changes along the curves in Figure 3, up to ~ 10 Hz for large k_{\perp} . Since the satellite is moving almost perpendicularly to the background magnetic field, the Doppler shift in the parallel direction can be neglected. The reconstructed wave distribution function is color coded (arbitrary units) and displayed on top of the dispersion curves. For comparison, in Figure 3b the temporal growth rate is color coded and placed on top of the dispersion curves. The instability is actually wider but only the region of large growth is shown. Notice that the dispersion curves shown are only those corresponding to $f = 0.983 f_{cH^+}$. Figure 3b is different from Figure 2, which shows constant frequency contours in the plasma reference frame, without Doppler shift.

[30] Comparing Figures 3a and 3b, we conclude that reconstructed WDF has a maximum close to the region in wave vector space where the waves are most unstable. Linear theory predict unstable waves with a wavelength of roughly 2.5 km and this is also what the reconstruction suggests. The maximum of the reconstructed WDF and the maximum temporal growth rate are, however, shifted a factor of 2 in k_{\parallel} . The reconstructed WDF is highly structured in the azimuthal direction, which is shown in Figure 3c. FAST is moving in the $\phi = 90^\circ$ direction and the WDF maximum occur in a direction oblique to the satellite trajectory.

[31] Figures 4a–4c shows the corresponding reconstruction results for $f = 1.026 f_{cH^+}$ (192 Hz). We observe a similar k_{\parallel} shift as for $f = 0.98 f_{cH^+}$ and the structure in the azimuthal direction is the same, with a peak at $\phi = 150^\circ$. We can conclude that we find solutions (that is, wave energy distributions) consistent with the wave data both above and below f_{cH^+} . However, to make the runs converge for $f = 1.026 f_{cH^+}$, we must in general allow a larger difference between the reconstructed spectra and the spectra we obtain from the data. There is also a tendency that the wave energy is located at larger k_{\perp} for $f = 1.026 f_{cH^+}$.

6. Discussion

[32] Our analysis shows a good agreement between the unstable region and the peak of the reconstructed WDF. This agreement suggests that the waves are generated

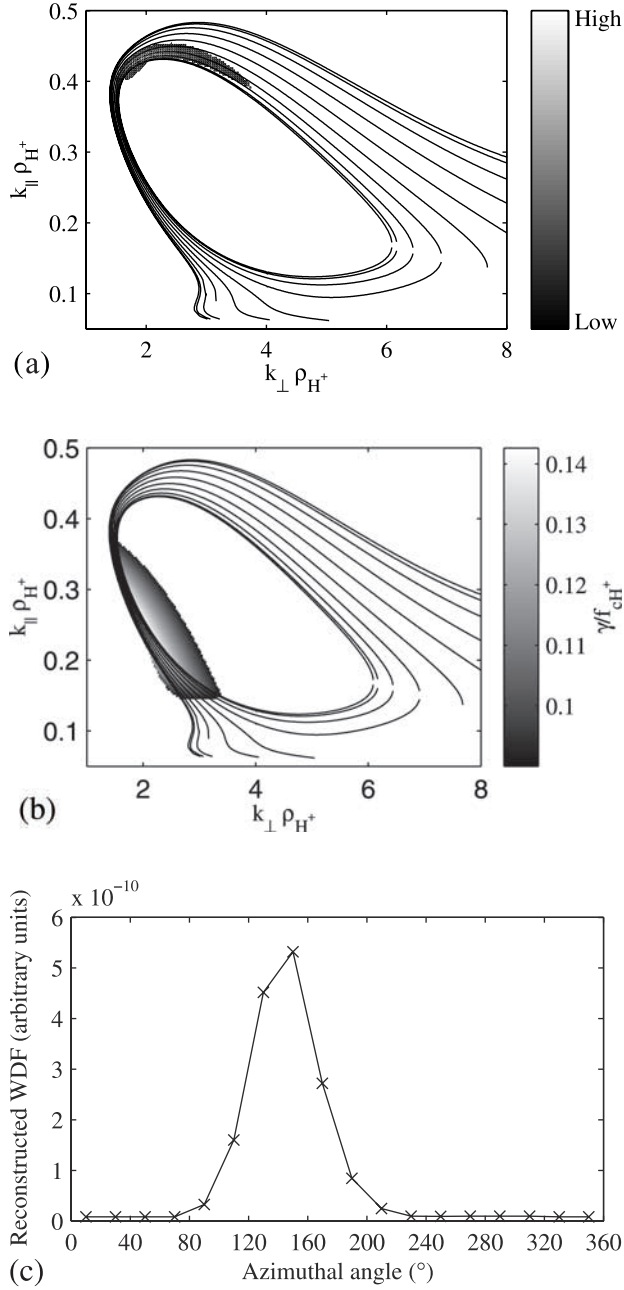


Figure 4. (a) The reconstructed WDF (arbitrary units) at frequency $f = 1.03f_{cH^+}$ (192 Hz) is shown on top of the dispersion relation. In the color code used red corresponds to much wave energy and blue to less wave energy. The solution to the dispersion relation is shown in the frame of reference of the satellite. Hence the different curves correspond to different directions of k_{\perp} (different ϕ). (b) The temporal growth rate is shown on top of the dispersion curves. (c) The reconstructed WDF versus azimuthal angle, ϕ . $\phi = 90^\circ$ is the direction of the satellite velocity.

locally, which also is consistent with the fact that the waves are found very close to multiples of the proton gyrofrequencies.

[33] The most obvious difference between Figures 3a and 3b and between Figures 4a and 4b is the shift in k_{\parallel} . To

investigate this shift between the WDF and the growth rate we set up model problems. In a model reconstruction we start from a WDF of our choice, that is, we decide where in \mathbf{k} space to put wave energy. In the next step we compute the autospectra and the cross spectra that this energy distribution produces and use these spectra as input to the reconstruction program. The model spectra are assumed to have a relative error of 10%, but no noise is added. This means that the model WDF satisfies $\xi[\psi] = 0$.

[34] Results from the model runs are presented in Appendix B (Figure B1). Only the result from a run with $f = 1.026 f_{cH^+}$ is presented, but the result for $f = 0.98 f_{cH^+}$ is similar and the discussion below applies to both cases. Starting from a situation where the wave energy is located in the region of maximum growth, we see that reconstruction is tending to put wave energy at larger (and smaller) k_{\parallel} . The reason for this lies in the way the reconstruction scheme is constructed. The entropy is defined so that $H[\psi]$ can be made to increase by spreading the energy over a larger volume in \mathbf{k} space. When setting up the reconstruction each point in \mathbf{k} space is assigned a volume. Without going into details, this volume scales with k_{\perp} (due to the use of cylindrical coordinates) and the inverse of the group velocity (due to the fixed frequency resolution $\Delta\omega$). In the presented model problem, energy is shifted toward regions in \mathbf{k} space with both larger k_{\perp} and smaller group velocity. That this is a feature of the reconstruction scheme can be seen by lowering the assumed relative error. When solving the model problem with smaller and smaller errors, the reconstructed WDF eventually approaches the model WDF. In order to test if this feature of the reconstruction scheme causes the shift between the instability and the WDF reconstructed from real data one could try to decrease the estimated variances of the observer frequency spectra. We have done this, but no solution for which $\xi[\psi] = 0$ exists in any of the cases we have studied, and solutions minimizing ξ becomes spiky and very sensitive to the exact value of ξ . Thus the model problem indicates that the observed shift in k_{\parallel} between the reconstructed WDF and the unstable region of \mathbf{k} space is due to a feature of the reconstruction scheme but does not offer a way to test this. Instead, to investigate the cause of the shift further, we introduce a form of biased reconstruction first described by [Oscarsson and Rönmark, 1990].

[35] A biased reconstruction means that the entropy is defined so that its global maximum is not obtained for $\psi = \text{const}$, but rather for a WDF having some predefined structure. The predefined structure in our case is a solution that is proportional to $\exp[\gamma(\mathbf{k})\Gamma]$, where Γ is a tuning parameter. This means that when the observed wave polarization puts little constraint on ψ , the reconstructed WDF will have a maximum in the region of \mathbf{k} space corresponding to the strongest instability. Figures 5a and 5b presents the WDF obtained by using a biased reconstruction, and in this case the reconstructed WDF indeed has its maximum in the region of maximum growth. The solution in Figure 5 should be compared with the unbiased solutions in Figure 3a and Figure 4a, and it should be emphasized that both solutions are equally consistent with the observed wave fields. Although we cannot draw any definite conclusions, the result of the model problem and the fact the biased

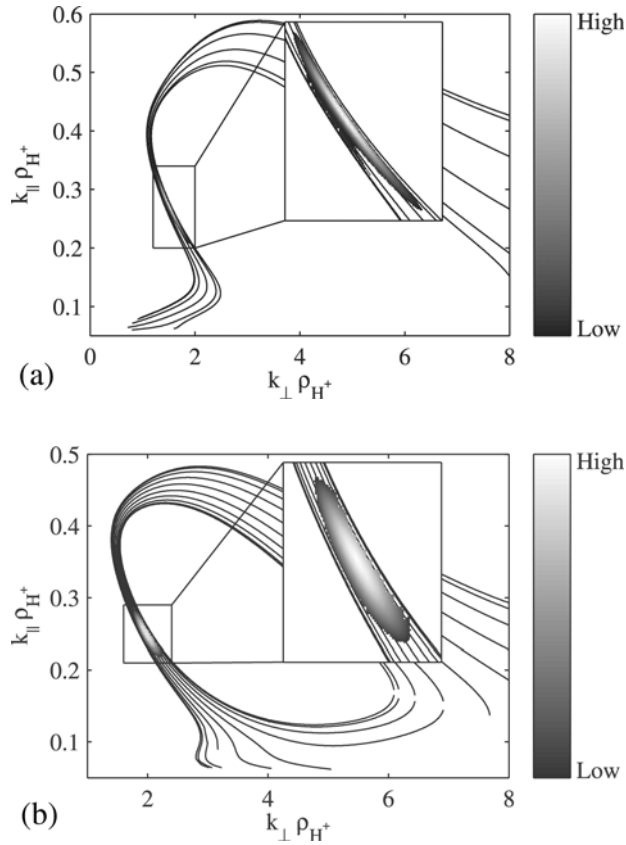


Figure 5. (a) The reconstructed WDF (arbitrary units) at frequency $f = 0.983f_{cH^+}$ (184 Hz) on top of the dispersion relation. The WDF is obtained using a biased reconstruction, which favors wave energy in the region of large growth. Should be compared to Figure 3a. (b) Biased reconstruction of the WDF at $f = 1.03f_{cH^+}$. Should be compared to Figure 4a.

reconstruction is confined to the unstable region of \mathbf{k} space, indicates that the shift in $k_{||}$ that we observe in the unbiased solution is caused by a feature of our reconstruction scheme.

[36] There are small differences between the results on the two different frequencies. However, to obtain solutions for the frequency above f_{cH^+} , we have to assume somewhat larger errors. We believe this is due to the left circularly polarized component present in the data. To see that such a component exists consider the spectral densities shown in Table A1. The imaginary part of the cross spectra between E_x and E_y is far from zero, indicating that a circularly polarized part is present. The sign of S_{i,E,E_y} reveals the sense of rotation, where a minus sign corresponds to left hand rotation.

[37] Theoretically, the growing waves are nearly linearly polarized, and we interpret the observations as being a combination of the growing wave mode and the left-hand polarized mode, which we find below f_{cH^+} at small k_{\perp} . We include the left-hand mode in the reconstruction, and we see that some of the wave energy is placed there. At $1.03f_{cH^+}$, there is no left-hand polarized mode to include, and we have no explanation of the presence of a left circularly component at this frequency. However, the reconstruction still

works; that is, we are able to find a solution consistent with the observations as long as we increase the estimated errors slightly.

[38] The results presented in section 5 are obtained with two different sets of spectral densities corresponding to different frequencies. However, the spectral densities depend not only on frequency but also on the data set chosen. To investigate this dependence, reconstructions are made with both shorter and longer data sets starting at 1947:40.417 UT. (The spectra used in section 5 were obtained using data from 1947:40.417 to 1947:43.104 UT.) Both the spectral densities obtained and the reconstructed WDF show very small differences compared to the results presented above in section 5. The coherence is low for all cases.

[39] Concentrating on the last part of the wave emission starting at 1947:42.614 UT, we discover somewhat larger differences. This part of the data is characterized by a considerably larger E/B than at the beginning of the event. The observed $E/B = 10c$ at $1.03f_{cH^+}$, which should be compared to $E/B = 2c$ at $1.03f_{cH^+}$ at the beginning of the wave emission. Below f_{cH^+} the corresponding values are $E/B = 5c$ toward the end of large emissions and $E/B = 0.8c$ at the beginning. A larger ratio E/B is more in accordance with the theoretical model, at least above f_{cH^+} , where our model predicts ratios above $3c$. Hence, above f_{cH^+} , it is easier to find solutions using data from the end of the wave event than it is using data from the beginning, that is, the estimated errors can be kept smaller. However, the reconstructed WDF does not look very different than the WDF obtained with data starting from 1947:40.417 UT. Below f_{cH^+} , it is no easier to reconstruct the WDF using data from the last part of the wave emission, rather the opposite. The solution is more spread out than it is using other data sets but the azimuthal angle distribution of wave energy remains the same.

[40] We conclude that results are insensitive to the particular choice of data set, which suggests our reconstruction method is a reliable method for analyzing this wave event. However, we want to investigate how sensitive the results are to variations of the plasma model as well.

[41] Keeping all other parameters as in Table 1, we vary the electron drift velocity v_e in the interval $2.2v_{th}$ to $2.5v_{th}$. Decreasing v_e lowers the frequency of the whole dispersion surface. Thus smaller drift velocities than $2.2v_{th}$ cause some azimuthal angles to disappear owing to the Doppler shift associated with the spacecraft motion. We find no solution for such azimuthal angles since the local maximum in $\omega(\mathbf{k})$ drops below f_{cH^+} . When the drift velocity is larger than $2.5v_{th}$, there is a growing broadband beam-like mode present as mentioned in section 3.

[42] Apart from the change in frequency, increasing v_e from $2.2v_{th}$ to $2.5v_{th}$ also shifts the instability slightly toward smaller $k_{||}$. The dispersion surface can only be found in the vicinity of the instability, and as the region of unstable waves moves, the dispersion surface itself moves with it. The reconstructed WDF follows the surface and is also shifted to smaller $k_{||}$. Apart from this shift in $k_{||}$, no major differences can be found between the results for the different plasma models.

[43] The effect of changing the ion beam velocities is similar. Increasing the ion velocities lowers the whole dispersion surface as previously discussed in section 3.

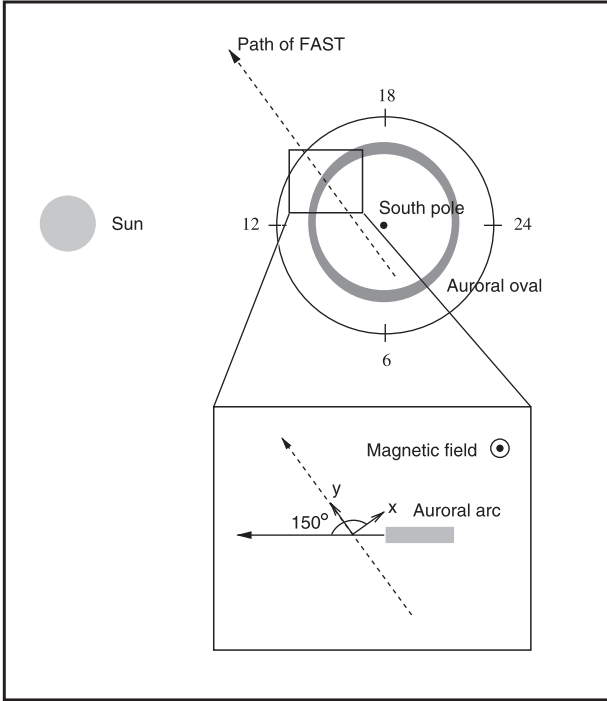


Figure 6. A suggestion of how to interpret the azimuthal angle distribution of wave energy. FAST is passing the edge of an auroral arc and the wave energy comes mostly from the direction along the arc. Waves from this direction have been able to grow as they spend long time in a region where the instability exists.

Nothing dramatic happens to the reconstructed WDF though. The angle distribution of wave energy is the same and the shifts in k_{\perp} and k_{\parallel} simply reflect the shift of the dispersion surface.

[44] Recent studies indicate that details of the electron distribution function [Chaston *et al.*, 2002] or gradients in the parallel ion beam velocities [Gavrishchaka *et al.*, 2000] are important for explaining higher multiples in the wave spectrum. Even though our simplified plasma model is unable to reproduce emissions at higher frequencies, we believe it is adequate for analyzing the polarization properties of waves close to the first multiple. By reconstructing the WDF we can analyze to what extent the observed wave fields are consistent with theoretical predictions, and simultaneously we obtain information about the dominant wavelength as well as the propagation direction of the waves. The wavelength that we obtain, ~ 2.5 km or a few times ρ_{H^+} , agrees with earlier estimates [Chaston *et al.*, 1998] and the peak in the azimuthal direction at $\phi \approx 150^\circ$ lends itself to a simple geometrical interpretation, as demonstrated in Figure 6. In this picture the emission is recorded in or close to an auroral arc, and waves propagating along the arc will have had time to grow to higher amplitudes than waves propagating across. Hence the WDF is dominated by waves propagating in the direction of the arc. This creates an asymmetry in the azimuthal distribution of wave energy, and this is what we observe in the reconstructed WDF. The situation in Figure 6 is oversimplified and requires the arc to be oriented at

about 45° relative to the auroral oval but this is not improbable.

7. Summary and Conclusions

[45] We have analyzed polarization properties of electric and magnetic wave fields observed by the FAST satellite in the southern auroral region. The analysis, which is based on reconstruction of the wave distribution function (WDF), provides information about characteristic wave lengths as well as propagation directions of the waves. Some features in the data, such as the appearance of spectral peaks at higher multiples of the proton gyrofrequency, f_{cH^+} , and a relatively large wave magnetic field slightly above f_{cH^+} , seem difficult to explain within the plasma model that we use. However, the fact that we find feasible solutions imply that overall, the observations are consistent with linear waves in a homogeneous plasma. Also, comparing with results from an accompanying analysis of the stability of the ambient plasma, we find good agreement between the reconstructed WDF and the proposed instability, supporting the precipitating electrons as the source of free energy. The analysis gives a wavelength of ~ 2.5 km, and the propagation direction obtained from the reconstructed WDF fits into a simple geometric picture, in

Table A1. Observed Spectral Densities^a

Spectrum	Spectral Density	Variance
<i>Frequency: 184 Hz</i>		
S_{B_x, B_x}	501.9	37.9
S_{B_y, B_y}	528.4	54.5
S_{B_z, B_z}	6.08	0.42
S_{r_x, B_y}	-218.0	37.8
S_{i_x, B_y}	-27.9	26.7
S_{r_y, B_z}	18.8	3.50
S_{i_y, B_z}	-2.04	3.83
S_{r_x, B_z}	-26.5	3.64
S_{i_x, B_z}	4.43	3.03
S_{E_x, E_x}	32.1	2.78
S_{E_y, E_y}	18.9	2.04
S_{E_z, E_z}	1.41	0.14
S_{r_x, E_y}	-5.34	1.37
S_{i_x, E_y}	-4.10	1.14
S_{r_y, E_z}	1.25	0.32
S_{i_y, E_z}	-1.88	0.31
S_{r_x, E_z}	-4.53	0.56
S_{i_x, E_z}	0.22	0.35
<i>Frequency: 192 Hz</i>		
S_{B_x, B_x}	159.4	10.1
S_{B_y, B_y}	83.0	7.74
S_{B_z, B_z}	2.69	0.22
S_{r_x, B_y}	4.07	5.95
S_{i_x, B_y}	-10.3	6.81
S_{r_y, B_z}	-0.71	0.94
S_{i_y, B_z}	-3.20	0.74
S_{r_x, B_z}	-8.89	1.16
S_{i_x, B_z}	-1.81	1.07
S_{E_x, E_x}	44.6	4.29
S_{E_y, E_y}	34.3	2.71
S_{E_z, E_z}	1.74	0.18
S_{r_x, E_y}	-22.3	2.28
S_{i_x, E_y}	-14.5	2.34
S_{r_y, E_z}	4.39	0.48
S_{i_y, E_z}	-2.35	0.40
S_{r_x, E_z}	-7.21	0.85
S_{i_x, E_z}	0.018	0.2

^aThe electric field spectral densities are given in $(\text{mV/m})^2/\text{Hz}$, and the magnetic field spectral densities are given in $(10^{-3} \text{ nT})^2/\text{Hz}$.

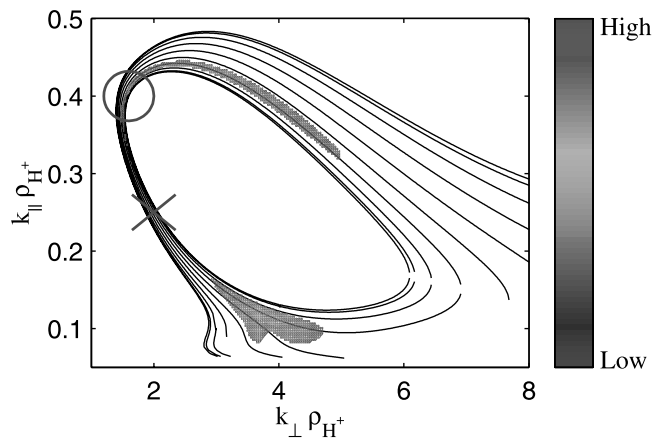


Figure B1. Resulting WDF from a model run at $f = 1.03 f_{cH^+}$. The model WDF is a very sharp peak (Gaussian) marked by a cross. The peak in the resulting WDF is difficult to see, and it is indicated by a circle.

which the satellite is passing obliquely through the outer edge of a region with precipitating electrons.

Appendix A: Spectral Densities

[46] In Table A1 we present the power spectral densities used in the WDF reconstructions together with the variances of the computed FFT spectra. S_{E_x, E_y} denotes the cross spectrum between the x and y component of the electric field. Indices r and i refer to the real and imaginary part of the cross-spectral densities. Note that all autospectral densities are real. A similar notation is used for the other spectral densities. The electric field spectral densities are given in $(\text{mV/m})^2/\text{Hz}$ and the magnetic field spectra in $(10^{-3}\text{nT})^2/\text{Hz}$. Spectra are calculated for the time period 1947:40.417–1947:43.104 UT.

Appendix B: Model Runs

[47] A model problem is set up by defining a model WDF (a Gaussian in this case) and computing the spectral densities from equation (2). These synthetic data are then used as input to the reconstruction method, and comparing the WDF reconstructed from the model spectra with the original model WDF tells us something about how the reconstruction method behaves. Figure B1 shows the outcome of a model run for the waves of interest in this paper. In this run we assume 10% errors in the synthetic spectra, but no noise is actually added. The model WDF is sharply peaked at the point marked by a cross in Figure B1, while the reconstructed WDF is color coded with dark blue corresponding to the lowest and red to the highest values (arbitrary units). Also, the reconstructed WDF is sharply peaked, and the color coding is somewhat difficult to see. Therefore the maximum of the reconstructed WDF is marked by a circle.

[48] The reconstructed WDF differs from the model in two obvious ways. First, the former is split into two parts, a minor peak (at $k_{\parallel} \rho_{H^+} \approx 0.1$) and a main peak (at $k_{\parallel} \rho_{H^+} \approx 0.4$), while the latter has a single peak (at $k_{\parallel} \rho_{H^+} \approx 0.25$). Second, the main peak in the reconstructed WDF is shifted toward larger k_{\parallel} compared to the model. Although different, it

should be emphasized that the reconstructed WDF and the model WDF are both consistent with the synthetic data. We believe that the differences arise owing to the entropy function that tends to spread energy over a large volume in \mathbf{k} space. Here the volume element associated with each point in \mathbf{k} space scales with k_{\perp} , owing to the use of cylindrical coordinates, and with the inverse of the group velocity, due to the finite frequency resolution. In the reconstructed WDF, energy is shifted to regions of both larger k_{\perp} and smaller group velocity, and hence the reconstructed WDF fills a much larger volume in \mathbf{k} space than the original model WDF. When the assumed errors are decreased, the reconstructed WDF approaches the model, indicating that the observed differences are due to features of the reconstruction scheme.

References

- André, M., Dispersion surfaces, *J. Plasma Phys.*, 33, 1–19, 1985.
- André, M., et al., Ion waves and upgoing ion beams observed by the Viking satellite, *Geophys. Res. Lett.*, 14, 463–466, 1987.
- Bendat, J. S., and A. G. Piersol, *Random Data: Analysis and Measurement Procedures*, John Wiley, New York, 1971.
- Bergmann, R., Electrostatic ion (hydrogen) cyclotron and ion acoustic wave instabilities in region of upward field-aligned current and upward ion beams, *J. Geophys. Res.*, 89, 953–968, 1984.
- Carlson, C. W., et al., The fast auroral snapshot (FAST) mission, *Geophys. Res. Lett.*, 25, 2013–2016, 1998.
- Carlson, C. W., et al., The electron and ion plasma experiment for FAST, *Space Sci. Rev.*, 98, 33–66, 2001.
- Cattell, C., et al., ISEE 1 observations of electrostatic ion cyclotron waves in association with ion beams on auroral field lines from 2.5 to 4.5 R_E , *J. Geophys. Res.*, 96, 11,421–11,439, 1991.
- Cattell, C., et al., The association of electrostatic ion cyclotron waves, ion and electron beams and field-aligned currents: FAST observations of an auroral zone crossing near midnight, *Geophys. Res. Lett.*, 25, 2053–2056, 1998.
- Chaston, C. C., et al., Characteristics of electromagnetic proton cyclotron waves along auroral field lines observed by FAST in region of upward current, *Geophys. Res. Lett.*, 25, 2057–2060, 1998.
- Chaston, C. C., et al., Electromagnetic ion cyclotron waves at proton cyclotron harmonics, *J. Geophys. Res.*, 10.1029/2001JA900141, 2002.
- Ergun, R. E., et al., The FAST satellite fields instrument, *Space Sci. Rev.*, 98, 67–91, 2001.
- Gavrishchaka, V. V., et al., Multiscale coherent structures and broadband waves due to parallel inhomogeneous flows, *Phys. Rev. Lett.*, 85, 4285–4288, 2000.
- Kaufmann, R. L., and P. M. Kintner, Upgoing ion beams, 1 Microscopic analysis, *J. Geophys. Res.*, 87, 10,487–10,502, 1982.
- Kintner, P., et al., Simultaneous observations of energetic (keV) upstreaming and electrostatic hydrogen cyclotron waves, *J. Geophys. Res.*, 84, 7201–7212, 1979.
- Klumpar, D. M., et al., Time of flight Energy, Angle, Mass Spectrograph (TEAMS) experiment for FAST, *Space Sci. Rev.*, 98, 197–219, 2001.
- McFadden, J. P., et al., Electron modulation and ion cyclotron waves observed by FAST, *Geophys. Res. Lett.*, 25, 2045–2049, 1998.
- McFadden, J. P., et al., Ion and electron characteristics in auroral density cavities associates with ion beams: No evidence for cold ionspheric plasma, *J. Geophys. Res.*, 104, 14,674–14,682, 1999.
- Oscarsson, T., Dual principles in maximum entropy reconstruction of the wave distribution function, *J. Comput. Phys.*, 110, 221–233, 1994.
- Oscarsson, T., and K. Rönmark, A combined wave distribution function and stability analysis of Viking particle and low-frequency wave data, *J. Geophys. Res.*, 95, 21,187–21,202, 1990.
- Oscarsson, T., et al., Towards a consistent picture of the generation of electromagnetic ion cyclotron ELF waves on auroral field lines, *J. Geophys. Res.*, 102, 24,369–24,386, 1997.
- Rönmark, K., WHAMP: Waves in homogeneous, anisotropic multi-component plasmas, *Rep. 179*, Kiruna Geophys. Inst., Kiruna, Sweden, 1982.

M. André, Swedish Institute of Space Physics, Uppsala Division, Box 537, SE-751 21 Uppsala, Sweden.

C. C. Chaston, Space Sciences Laboratory, University of California, Berkeley, CA 94720, USA.

T. Oscarsson and G. Stenberg, Department of Theoretical Physics, Umeå University, Umeå SE-901 87, Sweden. (gabriella.stenberg@space.umu.se)